

Geophysical Research Letters



RESEARCH LETTER

10.1029/2021GL092446

Key Points:

- Experimental determination of lower mantle melting relations and phase diagram by laser-heated diamond anvil cell
- One third of a pyrolytic magma ocean would first crystallize iron-depleted bridgmanite, than contains a substantial amounts of calcium
- Calcium concentration in liquidus bridgmanite is constant from 52 to 129 GPa, and delays the crystallization of calcium-silicate perovskite

Supporting Information:

Supporting Information may be found in the online version of this article.

Correspondence to:

J. Badro,
badro@ipgg.fr

Citation:

Nabiei, F., Badro, J., Boukaré, C.-É., Hébert, C., Cantoni, M., Borensztajn, S., et al. (2021). Investigating magma ocean solidification on Earth through laser-heated diamond anvil cell experiments. *Geophysical Research Letters*, 48, e2021GL092446. <https://doi.org/10.1029/2021GL092446>

Received 8 JAN 2021

Accepted 22 MAY 2021

Investigating Magma Ocean Solidification on Earth Through Laser-Heated Diamond Anvil Cell Experiments

Farhang Nabiei^{1,2}, James Badro^{3,1} , Charles-Édouard Boukaré^{1,3}, Cécile Hébert², Marco Cantoni⁴, Stephan Borensztajn³, Nicolas Wehr³, and Philippe Gillet¹ 

¹Earth and Planetary Science Laboratory, EPFL, Lausanne, Switzerland, ²Electron Spectrometry and Microscopy Laboratory, EPFL, Lausanne, Switzerland, ³Université de Paris, Institut de Physique du Globe de Paris, CNRS, Paris, France, ⁴Interdisciplinary Centre for Electron Microscopy, EPFL, Lausanne, Switzerland

Abstract We carried out a series of silicate fractional crystallization experiments at lower mantle pressures using the laser-heated diamond anvil cell. Phase relations and the compositional evolution of the cotectic melt and equilibrium solids along the liquid line of descent were determined and used to assemble the melting phase diagram. In a pyrolytic magma ocean, the first mineral to crystallize in the deep mantle is iron-depleted calcium-bearing bridgmanite. From the phase diagram, we estimate that the initial 33%–36% of the magma ocean will crystallize to form such a buoyant bridgmanite. Substantial calcium solubility in bridgmanite is observed up to 129 GPa, and significantly delays the crystallization of the calcium silicate perovskite phase during magma ocean solidification. Residual melts are strongly iron-enriched as crystallization proceeds, making them denser than any of the coexisting solids at deep mantle conditions, thus supporting the terrestrial basal magma ocean hypothesis (Labrosse et al., 2007).

Plain Language Summary The first 100 million years of Earth's history saw the mantle extensively molten by energetic impacts during its formation. How this melt solidified (i.e. from the bottom up or from the top down?) and the composition and signature of the "primitive" solid mantle it produced depend on the crystallization sequence of molten mantle silicates at large depths. In order to constrain this experimentally, we compressed and melted silicates whose composition is relevant to the bulk mantle, and then let them crystallize, using the laser-heated diamond anvil cell. We established the melting phase diagram of mantle silicates at 52 GPa (1300 km depth, a minimum for Earth's magma ocean), and show that about 1/3rd of the molten mantle solidifies to a buoyant mineral, calcium-bearing iron-poor bridgmanite, pushing the denser liquid downwards. Additional experiments up to 129 GPa show that this behaviour is observed up to core-mantle boundary conditions. This experimentally supports the terrestrial basal magma ocean hypothesis where the Earth's molten mantle crystallized from the top down, with the last remnants of melt located deep in the mantle, and challenges earlier bottom-up scenarios. Our experiments also support the formation of primitive bridgmanite mantle structures with a peculiar geochemical signature.

1. Introduction

The solidification of Earth's primitive molten silicate mantle (i.e., magma ocean) is, volumetrically speaking, the most important magmatic differentiation event in Earth's history (Elkins-Tanton, 2012; Solomatov, 2015). Despite taking place in the immediate aftermath of Earth's accretion ~4.5 Gyrs ago (Murthy, 1991), present-day observations have been linked to this event, because solidification (or melting) play a major role in the differentiation of terrestrial planets (Bowen, 1912), through the production of phases of distinct composition and density that are prone to gravitational segregation and geochemical isolation (Boukaré et al., 2015; Solomatov & Stevenson, 1993). The isotopic signature of basalts and mantle-derived rocks show evidence (Boyet, 2005; Mukhopadhyay, 2012; Mundl et al., 2017; Rizo et al., 2012; Touboul et al., 2012) for distinct geochemical reservoirs formed within the first 100 Myrs of Earth's history, and the current seismic structure above the core mantle boundary (CMB) suggests the presence (Dziewonski et al., 2010; Garnero & Jeanloz, 2000; Garnero & McNamara, 2008; Thorne & Garnero, 2004) of partially molten regions exhibiting compositional differences with the overlying mantle. Because of their old age and large depth, and because they have been geodynamically linked (Torsvik et al., 2010), these reservoirs/structures have been attributed

© 2021. The Authors.

This is an open access article under the terms of the [Creative Commons Attribution-NonCommercial License](https://creativecommons.org/licenses/by-nc/4.0/), which permits use, distribution and reproduction in any medium, provided the original work is properly cited and is not used for commercial purposes.

to silicate differentiation occurring during the solidification of a primordial magma ocean, and considered remnants of this primitive magma ocean (Labrosse et al., 2007).

In order to explain these geochemical and seismological observations by a process such as global magmatic differentiation, the petrological and geochemical evolution of magma ocean solidification has to be investigated experimentally. There has been significant efforts to study mineral-melt phase relations and trace element partitioning in mantle rocks (Corgne & Wood, 2004; Corgne et al., 2005; Liebske & Frost, 2012; Liebske et al., 2005; Walter et al., 2006) to pressure up to 26 GPa, corresponding to a depth of ~700 km in the mantle. However, the putative conditions of magma ocean crystallization on Earth are significantly deeper, a constraint obtained from core-formation modeling (Badro et al., 2015), a range where no experiments on phase relations have been performed to date: this goes from 1500-km depth for the most conservative models, all the way to the core-mantle boundary when accounting for the Moon-forming giant impact (Nakajima & Stevenson, 2015; Piet et al., 2017).

The present limitation on these experiments corresponds to the pressure limit of the multi-anvil press using tungsten carbide anvils, which is the standard tool to investigate phase diagrams at high pressures and temperatures (Ito, 2007). Typically in those experiments, a bulk starting composition is chosen, it is compressed and melted, and then cooled down to a given fraction of residual melt; it is then quenched, recovered, polished, and analyzed chemically and mineralogically using standard analytical tools such as the electron microprobe or scanning electron microscope (Ohtani et al., 1995). Repeating these experiments while varying the fraction of residual melt and using different starting compositions (Kogiso et al., 1998) then allows to probe and describe the mineral-melt phase relations and melting phase diagram.

While this is a routine experimental protocol in large-volume presses, and the preferred methodology for conducting such investigation with such experimental tools, a similar protocol has remained technically unmanageable in the laser-heated diamond anvil cell (LHDAC), the only tool reaching higher pressures and temperatures to cover all plausible conditions of magma ocean crystallization on Earth, for two reasons. The first stems from the inability to accurately control experimental conditions in the LHDAC at extreme conditions, specifically the precise control of temperature required to slowly crystallize the melt and attain controlled degrees of crystallization (e.g., fractions of residual melt). Second, the size of the phases produced in the LHDAC is nanometric, so that the analysis of the run products requires the use of high-resolution analytical techniques (Badro et al., 2007; Piet et al., 2016) that enable at least a 100-fold gain in spatial resolution.

Here, we have undertaken a novel approach to establish phase diagrams and melting relations in the LHDAC using three-dimensional (3D) quantitative focused ion beam (FIB) chemical analysis combined with analytical transmission electron microscopy (TEM). Our protocol consists in carrying out a series of experiments where samples are molten at a fixed pressure and then slowly cooled down and fractionally crystallized to various degrees in a narrow temperature range. We tracked the crystallization sequence of two silicate melts, one with an olivine starting composition, and one with a pyrolitic bulk composition. We were able to unambiguously determine the mineralogy and composition of liquidus phase, for example, the first mineral phase to crystallize in a cooling magma ocean, as well as the composition of the residual liquid. As crystallization proceeds, the liquid line of descent follows the cotectic melt composition while crystallizing equilibrium phases, whose mineralogy and composition are also measured, thus delineating the melting phase diagram in the MgO-FeO-SiO₂ pseudo ternary at 52 GPa.

2. Materials and Methods

Five melting/partial crystallization experiments (Table S1) were performed in the LHDAC at 52 GPa, using olivine or a “simplified” (i.e., restricted to FCMAS, the mantle’s major components: FeO-CaO-MgO-Al₂O₃-SiO₂) pyrolite as starting materials (Table S2). Pyrolitic glass was produced in a gas-mixing aerodynamic levitation laser furnace (IPGP) at 2050°C and an oxygen fugacity of IW+1.3. All samples were compressed to 45 GPa, then heated and molten using double-sided laser heating (IPGP). The samples were then allowed to cool down very slowly at a rate of 0.6–1 K/s (Figure S1), over the course of 30–360 s, to final temperatures in the 3000–3200 K range (*in situ* pressure reaching 52 GPa due to thermal pressure). Because of the constant cooling rate, longer experiments reach lower final temperature, and therefore have a lower residual

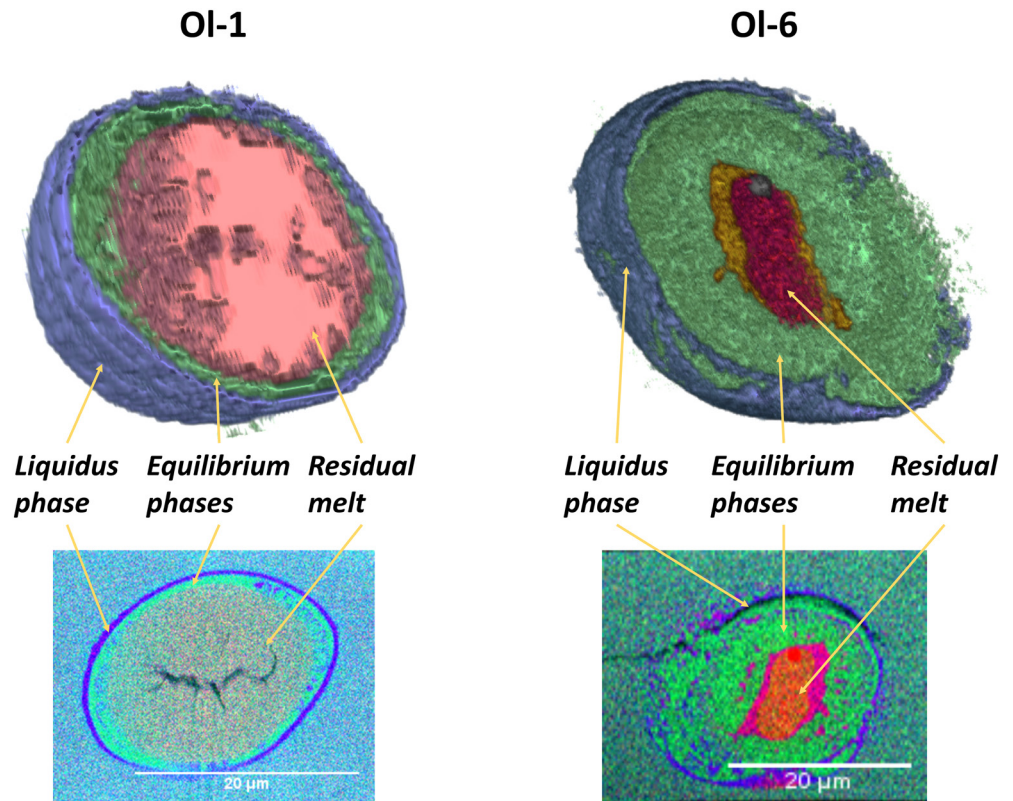


Figure 1. (top) 3D chemical (FIB EDS) tomographic reconstruction of samples OI-52-1 (left) and OI-52-6 (right) with olivine starting composition, and corresponding 2D chemical distribution of the central slice (bottom). Samples are molten at 52 GPa, and then cooled to different final temperatures to reach different. Each sample has outer rim (constituted of the liquidus phase, Fp in this case), an innermost core (the residual liquid), and in between a shell (made of the equilibrium phases Brg and Fp, crystallizing from the residual melt). As the residual melt fraction decreases, the size of the shell increases, while the liquidus phase rim remains identical in mineralogy, composition, and volume. The fact that two equilibrium phases (shell) are growing from the residual melt implies that the latter has reached a cotectic composition. FIB, focused ion beam.

melt fraction. Two additional experiments were produced at higher pressure (85 and 129 GPa) using pyrolite composition; the samples were once again first molten and then cooled to final temperatures of 3600 and 3900 K, respectively. The samples are then quenched by shutting off laser power (ramp down time $\sim 10 \mu\text{s}$) and decompressed, unloaded from the LHDAC, and transferred to a FIB instrument for sample recovery and analysis.

Zeiss NVision 40 and NVision X540 dual beam FIB instruments (EPFL) were used to mill through the sample until the laser-heated part was reached. Then, thin slicing, secondary electron imaging, and compositional (EDS) mapping were iterated until the center of the heated spot was reached, allowing to reconstruct tomographically the 3D volume (see supporting information), and to produce a 3D chemical and mineralogical model of the sample as shown in Figure 1. The FIB was then used to prepare a thin section from the center of the laser-heated region; it was lifted-out, transferred to a copper TEM grid and further thinned down to electron transparency to be analyzed on a FEI Tecnai Osiris scanning transmission electron microscope (STEM) equipped with four windowless Super-X SDD EDS detectors (EPFL) for elemental concentrations using K lines for quantification.

3. Results

The part of the sample that was molten and then recrystallized, hereafter called “melt pocket” (Figure S5), always has a spherical geometry, with a size $\sim 25 \mu\text{m}$ in diameter, consisting of large chemically/mineralogically differentiated concentric (Figures 1 and S9) ensembles. Outside of this melt pocket, the sample is

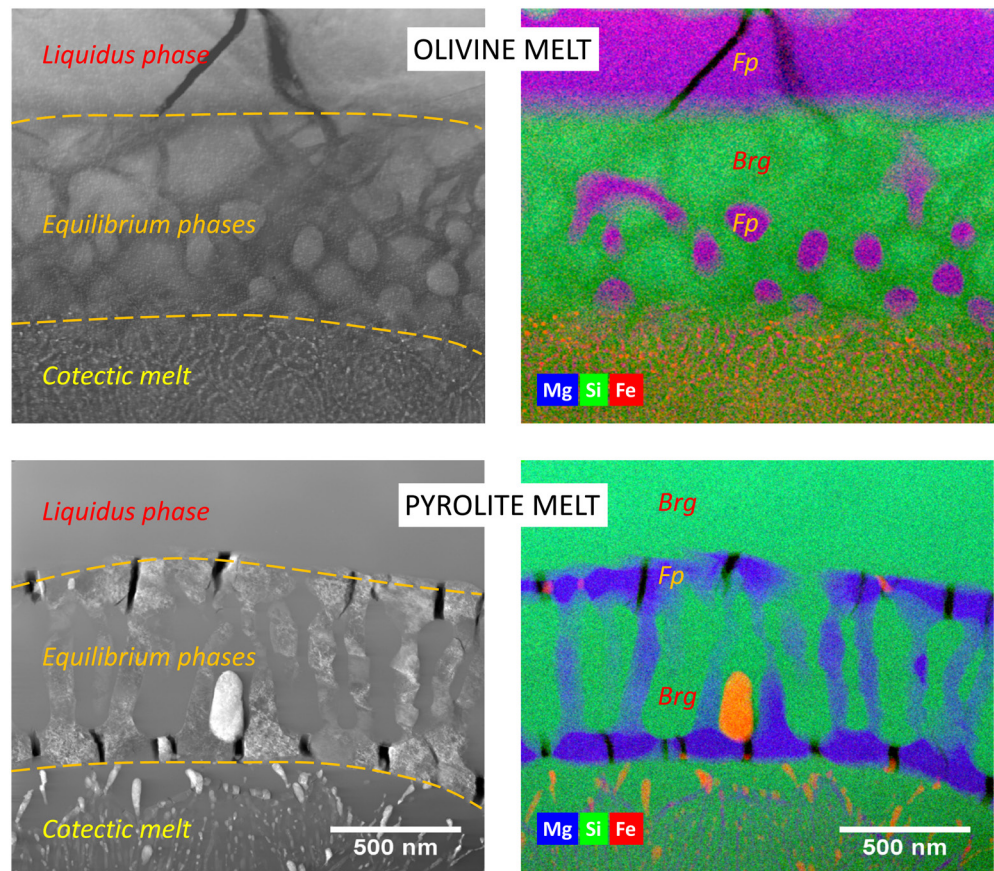


Figure 2. TEM high-angle annular dark field images (left) and the combined EDS chemical maps of Fe, Mg, and Si (right) for partially crystallized melts at 52 GPa, from an olivine and pyrolite bulk composition (runs Ol-52-1 and Pyr-52-1, respectively). The center of the sample is at the bottom (outside the field of view) and the sample is crystallizing from the top to the bottom (i.e., inwards toward the center). The rim is the liquidus phase (Fp for olivine composition, Brg for pyrolite composition). The shell is composed of both ferropericlase and bridgmanite, the equilibrium solid phases on the cotectic. The core is the residual melt, which has reached cotectic composition by virtue of the fact that the two equilibrium phases (Fp and Brg) are crystallizing from it. TEM, transmission electron microscopy.

constituted of unheated and untransformed glass, which recrystallizes as it approaches the edges of the melt pocket and temperature increases; the glass morphs continuously into a (Figure S2) nanometer-scale mineral assemblage, and multiple chemical analyses show compositions identical to that of the starting material, in the far-field untransformed glass as well as the recrystallized region in the vicinity of the melt pocket. This is clear indication of the absence of chemical exchange between the melt pocket and its surroundings asserts that it can be considered a closed chemical system, which is essential to interpret its petrological evolution as it crystallizes.

The melt pocket always shows three concentric parts, regardless of the starting melt composition (olivine or pyrolite). An outermost rim consisting of a single mineral phase (Fp for an olivine melt, Brg for a pyrolite melt), surrounding an intermediate shell consisting of a two-phase assemblage (Brg + Fp), itself surrounding the innermost central core showing no distinct large-scale mineralogy. These can be clearly identified in the elemental 3D reconstructions (Figure 1) and can be imaged and analyzed with greater detail and resolution using TEM analysis (Figures 2 and S3). The composition of these ensembles for the five samples is reported in Table S3.

The melt pocket's outermost rim is the liquidus phase (blue region in Figure 1), the first mineral phase crystallizing out of the melt as it cools. Our experiments confirm that at 52 GPa, Fp is the liquidus phase for an olivine composition melt, while Brg is that of a pyrolitic melt, as has been previously reported (Boukare et al., 2015; Fiquet et al., 2010). The volume and composition of the rim are constant regardless of the degree

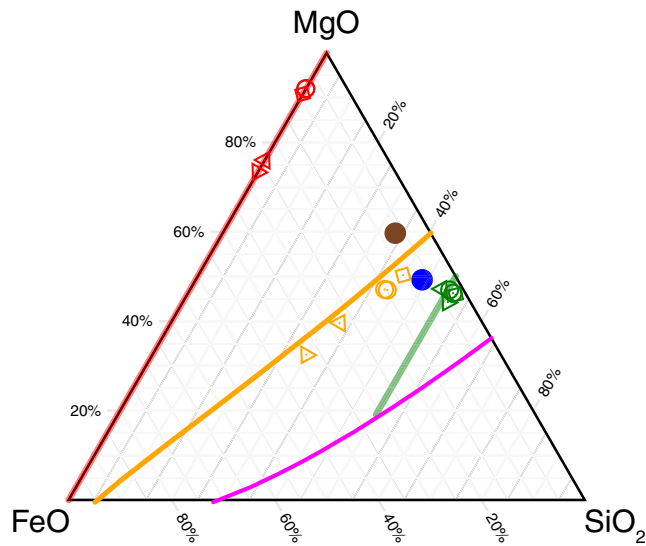


Figure 3. Calculated ternary FeO-MgO-SiO₂ phase diagram at 52 GPa (similar plot with liquidus isotherms shown in Figure S8). The maroon and blue circles represent the olivine and pyrolitic starting compositions, respectively. Melt core compositions measured by TEM EDS are plotted as yellow symbols—except for the Ol-52-3 sample that has been analyzed by FIB EDS only—and are in excellent agreement with the predicted cotectic melt line (yellow line) between the stability fields of ferropericlase and bridgmanite. Red and green symbols represent the compositions of ferropericlase and bridgmanite measured in the shell, that is, expected to be in thermodynamic equilibrium with the cotectic melt. Red and green lines highlight the ferropericlase and bridgmanite stoichiometric compositions. The purple line is the second cotectic in the phase diagram, laying between the stishovite and bridgmanite stability fields (reported for completeness, but not measured in our experiments). FIB, focused ion beam; TEM, transmission electron microscopy.

of crystallization of the melt. This can most clearly be seen in the olivine sequence where the residual melt fraction in the three experiments is 50%, 20%, and 2%.

The intermediate shell (green region in Figure 1) consists of a Brg and Fp assemblage (regardless of starting composition), the equilibrium phases along the cotectic in the FMS pseudo-ternary (Figure 3); their occurrence proves that the melt they are crystallizing from has reached the cotectic composition, which is further confirmed by fact that they are the same regardless of starting melt composition. The volume of this shell increases with the degree of crystallization of the melt (Figure 1) at the expense of the central part of the melt pocket.

Finally, the innermost core shows no large-scale minerals (apart from nanometer-scale quench texture) and no distinct composition. As crystallization proceeds, its volume shrinks and it is gradually iron-enriched. It represents the residual liquid prior to quench, and its volume fraction allows to obtain the final degree of residual melt in each experiment.

4. Interpretation

Altogether, these experiments prove that the melt crystallizes from the outside toward the center. The first phase to crystallize is the liquidus phase, and naturally constitutes the outermost rim. This rim is always monomineralic, as one expects for a liquidus phase; moreover it is different for the two starting melt compositions, as expected, because these are on opposite sides of the Fp-Brg cotectic (blue and brown circles + yellow line, in Figure 3) melt composition: olivine is on the Fp side of the cotectic so that Fp is the liquidus phase, while pyrolite is on the Brg side, with that phase being the liquidus.

Interestingly, the liquidus rim is significantly bigger in the pyrolite experiments than in the olivine experiments. This is a flawless illustration of the lever rule: at 52 GPa, pyrolite lies in the middle between the liquidus (Brg) and the cotectic melt composition (blue circle, Figure 3), implying that a large amount of Brg (33%–36% in modal abundance) needs to be crystallized before the liquid line of descent reaches the cotectic composition, and then starts crystallizing equilibrium solids (Brg + Fp). The olivine composition, on the other hand, is much closer to that cotectic melt composition than to its liquidus phase line (Fp), so that a small amount of Fp crystallization (17% in modal abundance) and removal from the melt suffices to push the residual liquid composition onto the cotectic.

Once the residual melt reaches the cotectic composition, it starts crystallizing simultaneously both equilibrium solids, Fp and Brg, and the melt follows the cotectic composition line of descent as crystallization proceeds. The fact that equilibrium solids are observed in all our crystallization sequences implies that all our residual melts are in fact also cotectic melts; therefore, their composition gives a direct sampling of that of the cotectic melt, which allows to draw the cotectic melt composition line in the ternary phase diagram (yellow line, Figure 3). As expected, the crystallization of the cotectic melt produces the same equilibrium phases regardless of starting melt composition, and the cotectic melt compositions from the pyrolite and olivine starting compositions are indistinguishable (Figure 3 and Table S3). Because calcium silicate perovskite (CaPv) phase is not observed in our pyrolite melt experiments (see Section 5), we can easily project the pyrolite data on the FMS pseudo-ternary phase diagram, and use it alongside the olivine data to construct the full melting phase diagram at 52 GPa (Figure 3).

Finally, the mode of crystallization in our experiments approaches fractional crystallization. If batch crystallization had been taking place, the composition and modal abundance of the liquidus phase would change as a function of residual melt fraction, which is not observed, on the contrary: The volume and composition

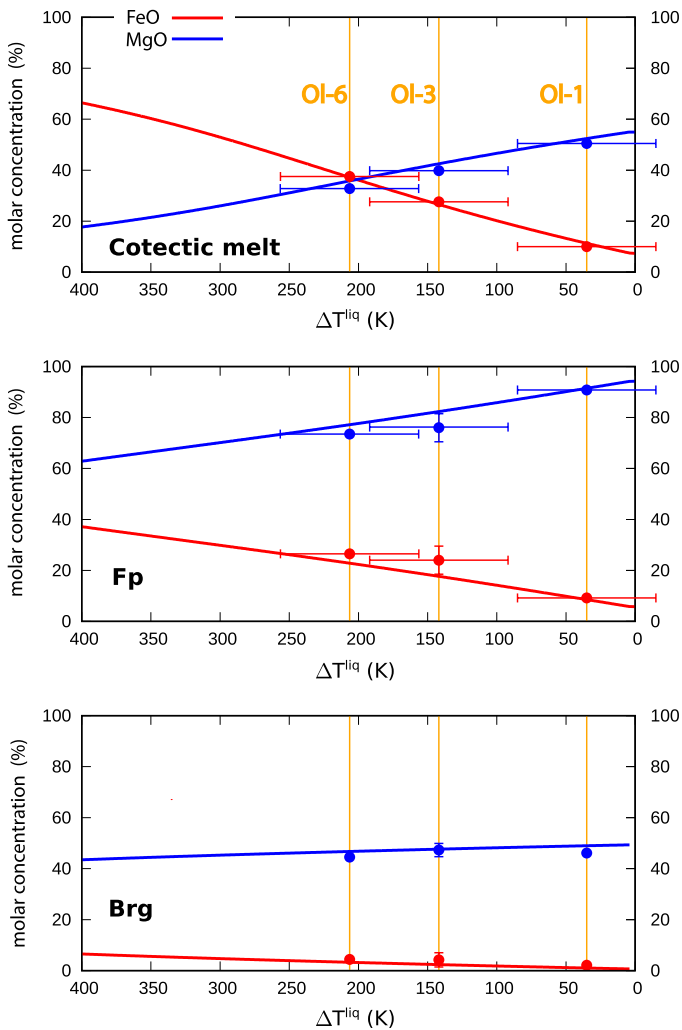


Figure 4. Composition of the cotectic melt (top) and equilibrium solids (Fp in the middle, and Brg at the bottom). The lines are obtained from a simulation (Boukare et al., 2015) of fractional crystallization sequence at 52 GPa, using the phase diagram (Figure 3). The horizontal axis corresponds reports temperature below the liquidus. The circles (uncertainty smaller than symbol size when not shown) are the experimental compositions from the OI-52 series (Table S3) and show remarkable agreement with the calculation. The three snapshots (OI-52-1, -3, and -6) of the crystallization sequence corresponds to 35, 145, and 205 K below the liquidus temperature of olivine melt at 52 GPa. Uncertainties on temperature are from Table S1, those on composition are from Figure S3. Temperature uncertainties are not plotted in the bottom panel (Brg composition) for lisibility's sake, but they are the same as those in the other two plots.

iron-enriched melt proceeds, the arising equilibrium solids become iron-enriched too, and their gradual iron enrichment along the crystallization sequence can be tracked (Figures 4 and S3). But despite this compositional variation, the exchange constant $K_D^{brg/fp} = \left(X_{Fe}^{brg} X_{Mg}^{fp} \right) / \left(X_{Fe}^{fp} X_{Mg}^{brg} \right)$ remains constant (Figure S3), and serves as a confirmation of local thermodynamic equilibrium conditions for the crystallization of these phases from the melt. Further comparison with subsolidus Fp-Brg iron partitioning experiments (Piet et al., 2016 and refs. therein) shows remarkable agreement, both for the olivine ($K_D = 0.3$) and pyrolite ($K_D = 0.6$) system.

of the liquidus phase is constant for the two crystallization sequences. The same logic applies for the composition and mineralogy of the equilibrium solids, which for each experiment, would depend on residual melt fraction; but for a given crystallization sequence, the outermost parts of the melt pocket that they have in common (not only the liquidus rim, but also the outermost part of equilibrium shell) are identical in mineralogy, composition, and volume. Finally, our most solidified samples (OI-52-3 and OI-52-6) would simply violate mass balance (Figure S10).

This is further confirmed by comparing our experimental results with a thermodynamically modeled crystallization sequence. A fractional crystallization sequence was calculated (see supporting information) for an olivine melt starting composition at 52 GPa, using the self-consistent thermodynamic model (Boukare et al., 2015) that underpins the calculated phase diagram (Figure 4). The composition of the cotectic melt and that of the two equilibrium solid phases (Brg and Fp) is calculated as a function of temperature. The experimental data (Table S3) is plotted alongside the calculated curves, and shows remarkable agreement, bringing an independent proof of fractional crystallization taking place in our LHDAC experiments. One should note, however, that the absolute temperatures predicted by the model are higher than the ones reported in our experiment, the origin of which is discussed in the supporting information.

As the melt pocket crystallizes from the outside inwards, solids stop participating chemically in the crystallization process, as if they were physically removed. This is reminiscent of the separation between the melt pocket as a whole and the surrounding sample during initial melting, and again can be attributed to the tremendous difference in diffusion coefficients (and therefore diffusion times) between solids and liquids. It is unclear if the solids could re-equilibrate with the residual melt should longer experiments be performed; but it is clearly not the case at the timescales (30–360 s) used in our protocol.

Finally, the two pyrolite samples were produced in similar conditions: Same pressure, same temperature, and roughly the same cooling time, in order to assess the reproducibility of our experiments. The morphology and the composition of the various phases (Table S3) for these two experiments are indistinguishable, proving the high reliability and repeatability of our experimental protocol.

5. Discussion

Our first observation is general, in that it applies regardless of melt composition: as crystallization progresses, residual melts are increasingly FeO-enriched and MgO- and SiO₂-depleted (see Table S3, Figures 3 and 4), which should make it significantly denser than coexisting solids (Ohtani et al., 1995). As the fractional crystallization of an increasingly

We can clearly attribute Brg as the liquidus phase for a pyrolitic melt at high pressure, as previously determined in melting experiments (Fiquet et al., 2010) and phase diagram studies (Liebske & Frost, 2012). The initial stage of the solidification of a terrestrial (pyrolitic) magma ocean at those depths should lead to the crystallization of large amounts of bridgmanite, estimated at 33%–36% from the phase diagram (Figure 3), prior to the crystallization of other solids. The compositional contrast between these first solids and the melt is quite stark in terms of iron concentration (Figure 4, Table S3), with an iron enrichment in the melt of $D_{\text{Fe}} = 0.2\text{--}0.33$: bridgmanite crystallizing as the liquidus phase contains 2.1 mol% FeO, while the melt starts at 7 mol%, and increases to 11 mol% as the iron-depleted bridgmanite component is removed from the melt. Therefore, the first solid cumulates crystallizing out of a deep magma ocean must be significantly more buoyant than the melt they are crystallizing from (Boukare et al., 2015), and should float while pushing the denser melt downwards, providing a strong petrological argument to form a basal magma ocean on Earth (Labrosse et al., 2007). Additionally, a recent geodynamical study has made the case for the existence of a bridgmanite-enriched deep mantle reservoir (Ballmer et al., 2017), as ancient structures called BEAMS inherited from magma ocean crystallization, that were (at least in part) preserved through geologic time despite entrainment and mixing by mantle convection. Our experiments show that large amounts (about one third of the magma ocean) of “primitive” bridgmanite can crystallize out of a pyrolitic magma ocean as it starts solidifying in the deep mantle. This “primitive” bridgmanite crystallizes prior to any other mantle phases, and therefore coexists solely with the melt, providing a petrological basis for ancient bridgmanite-rich mantle structures. The imposing size of this “primitive” bridgmanite reservoir is consistent with the fact that its remnants have survived through ~ 4.5 Gyr of mantle dynamics.

Interestingly, bridgmanite crystallizing out of a pyrolitic melt (2.4 mol% CaO) contains 44 mol% MgO and 2 mol% CaO, equivalent to a 4 mol% CaPv component. The Ca-incorporation in Brg has been theoretically debated (Jung & Schmidt, 2011; Vitos et al., 2006), and experimentally reported in several recent studies (L. S. Armstrong et al., 2012; Creasy et al., 2020; Kuwahara et al., 2018; Nomura et al., 2017). Our experiments add to this corpus of observations; they are fully consistent with crystallization experiments conducted at lower pressure (Nomura et al., 2017) showing significant (between 3 and 5 mol%) CaPv solubility in Brg at 25 GPa. In a pressure range similar to ours, the subsolidus equilibrium between Brg and CaPv (Creasy et al., 2020) shows increasing CaPv dissolution in Brg as the ferric/ferrous iron ratio in bridgmanite increases. In the synthesis conditions of our pyrolite glass (2050°C at IW+1.3 in a gas-mixing aerodynamical levitation laser furnace), our initial ferric iron concentration is $\sim 30\%$ (Sossi et al., 2020), intermediate between the reduced and oxidized samples studies in Creasy et al. (2020); interestingly, the Ca-concentration we measure in Brg are also intermediate between those observed in these subsolidus experiments, providing seamless consistency between these observations. Finally, the two experiments at higher pressures (85 and 129 GPa) were carried out (Figure S7) for the sole purpose of confirming this observation at all lower mantle pressures. The samples were slightly crystallized (very large degree of residual melt), so as to solidify only the liquidus phase (Brg), which has the same Ca concentration (Table S3) as those at 52 GPa, despite significantly higher P and T (see Table S1). This confirms that Brg remains the liquidus phase for pyrolite, and hence the first one to crystallize out of the melt, down to CMB pressure conditions, and demonstrates that it still contains substantial (and rather constant) amount of calcium at any lower mantle depth. No resolvable pressure dependence of the calcium solubility into Brg is observed here, but one should keep in mind that our experiments at 52, 85, and 129 GPa are not carried out at the same temperature, but below the pyrolite liquidus at each pressure. In this sense, they directly reflect the composition of Brg as it is crystallizing out of a pyrolite melt.

Such a significant intake of CaPv in primitive Brg will necessarily delay the mineralogical expression of CaPv as a rock-forming phase per se. Indeed, no traces of CaPv were found even as 66% of the melt had crystallized in our experiments. While the calcium concentration in the 34% residual melt (3.1 mol%) is higher than that in the starting pyrolitic melt (2.4 mol%), it is not nearly as high as one would expect from mass balance (7.2 mol%) if Brg had incorporated no calcium at all. The increasing calcium concentration in the melt leaves no doubt that CaPv will crystallize at a critical point during further solidification, but its substantial incorporation in Brg significantly delays this occurrence, and the expression of CaPv in the crystallization sequence. Crystallization experiments with a smaller degree of residual melt need to be carried out to determine the threshold at which CaPv starts crystallizing along the solidification sequence. Evaluating this is important for two essential reasons: First to pinpoint a critical residual melt fraction in Earth's

magma ocean after which notable disturbance in trace-element ratios, driven by CaPv crystallization (Caro et al., 2005; Corgne et al., 2005; Hirose et al., 2004; Liebske et al., 2005; Walter & Trønnes, 2004), is expected; and second to measure the calcium concentration in Brg at calcium saturation (i.e., CaPv crystallization) and compare it to our measured value of 2.1 mol% in primitive (i.e., crystallizing in the absence of CaPv) bridgmanite. As these two “generations” of bridgmanite could have stark difference in their trace-element concentration and ratios, they could constitute two deep terrestrial reservoirs with drastically different geochemical signature.

The abundance of certain trace elements, which are strongly fractionated by bridgmanite, have chondritic ratios in the BSE. On this basis, it has been argued that crystallizing large amounts of bridgmanite from a magma ocean is unlikely (Kato et al., 1988a, 1988b), unless it was accompanied by the crystallization of CaPv (Corgne et al., 2005; Walter & Trønnes, 2004), because those two minerals have opposite fractionation effects that compensate each other; this requires between 2.5% (Rizo et al., 2011) and 7% (Caro et al., 2005) CaPv to counterbalance the fractionation of Brg. The dissolution of 4% CaPv in Brg that we observed falls in this range, and relaxes the constraint for concomitant CaPv and Brg crystallization at the onset of magma ocean solidification, which is petrologically unlikely and undoubtedly unsupported by experimental investigation (our work + (Kuwahara et al., 2018; Nomura et al., 2017)).

Lastly, metallic iron is observed in the residual melts of both bulk compositions (Figure S4) that differ in their initial ferric iron content (no starting Fe^{3+} in olivine melt, and $\sim 30\%$ Fe^{3+} in pyrolite melt). This is indirect confirmation that high ferric-iron contents are thermodynamically favored at high pressures, as has recently been reported at upper mantle pressures (K. Armstrong et al., 2019), and seems to be the case up to at least to 52 GPa.

6. Conclusions

We have shown that we can reliably melt then crystallize silicate melts to various degrees of residual melt, at deep mantle conditions relevant to Earth's primitive molten mantle, using LHDAC experiments associated with FIB and TEM analytical investigation. The 3D compositional by FIB EDS allows to discriminate the different petrological ensembles, and reliably estimate their volume fractions. We were able to determine the composition of the cotectic melt line from both sides in the FeO-MgO-SiO₂ ternary, along with that of equilibrium solids crystallizing from it. We determined the liquidus phase in two parts of that phase diagram. The data was then used to describe the melting phase diagram in the FMS ternary system at 52 GPa. This paves the way to study melting relations, solid-melt equilibria, and phase diagrams for the deep mantle. This protocol can be extended to all pressure and temperature conditions attainable in the LHDAC, that routinely covers the whole range of mantle depths. Our work confirms that bridgmanite is the liquidus phase in a pyrolitic melt at mid-mantle pressures (Fiquet et al., 2010); it will be the first solid phase to crystallize in a deep magma ocean, will have low iron and substantial calcium concentration, and would constitute a large (1/3rd of the magma ocean) early mantle reservoir (Ballmer et al., 2017). The residual melt will evolve toward strong iron enrichment, making it unquestionably denser than coexisting solids, favoring its gravitational settling toward to core-mantle boundary, and giving rise to a deep-seated basal magma ocean (Labrosse et al., 2007).

Acknowledgments

The authors acknowledge Rick Ryerson, Richard Gaal, Duncan Alexander, Teresa Dennenwaldt, and Emad Oveisi for scientific and technical support, and the assistance of Fabienne Bobard and Danièle Laub in sample preparation. The research received funding from the Swiss National Science Foundation through FNS Grants 200021_169854 (J. Badro) and 200021_140474 (P. Gillet). This work has received funding from the European Research Council (ERC) under the European Union's Horizon 2020 research and innovation program (grant agreement no. 101019965—SEPTIM). Parts of this work were supported by IPGP multidisciplinary program PARI, and by Paris-IdF region SESAME Grant no. 12015908. J. Badro acknowledges the financial support of the UnivEarthS Labex program at Université de Paris (ANR-10-LABX-0023 and ANR-11-IDEX-0005-02).

Data Availability Statement

The experimental data used in this manuscript can be found in a FAIR-compliant data repository at <https://doi.org/10.5281/zenodo.4656784>.

References

- Armstrong, K., Frost, D. J., McCammon, C. A., Rubie, D. C., & Boffa Ballaran, T. (2019). Deep magma ocean formation set the oxidation state of Earth's mantle. *Science*, 365(6456), 903–906. <https://doi.org/10.1126/science.aax8376>
- Armstrong, L. S., Walter, M. J., Tuff, J. R., Lord, O. T., Lennie, A. R., Kleppe, A. K., & Clark, S. M. (2012). Perovskite phase relations in the system CaO-MgO-TiO₂-SiO₂ and implications for deep mantle lithologies. *Journal of Petrology*, 53(3), 611–635. <https://doi.org/10.1093/petrology/egr073>

- Badro, J., Brodholt, J. P., Piet, H., Siebert, J., & Ryerson, F. J. (2015). Core formation and core composition from coupled geochemical and geophysical constraints. *Proceedings of the National Academy of Sciences of the United States of America*, 112(40), 12310–12314. <https://doi.org/10.1073/pnas.1505672112>
- Badro, J., Ryerson, F. J., Weber, P. K., Ricolleau, A., Fallon, S. J., & Hutcheon, I. D. (2007). Chemical imaging with NanoSIMS: A window into deep-earth geochemistry. *Earth and Planetary Science Letters*, 262(3–4), 543–551. <https://doi.org/10.1016/j.epsl.2007.08.007>
- Ballmer, M. D., Houser, C., Hernlund, J. W., Wentzcovitch, R. M., & Hirose, K. (2017). Persistence of strong silica-enriched domains in the Earth's lower mantle. *Nature Geoscience*, 10(3), 236–240. <https://doi.org/10.1038/ngeo2898>
- Boukare, C. E., Ricard, Y., & Fiquet, G. (2015). Thermodynamics of the MgO-FeO-SiO₂ system up to 140 GPa: Application to the crystallization of Earth's magma ocean. *Journal of Geophysical Research: Solid Earth*, 120(9), 6085–6101. <https://doi.org/10.1002/2015JB011929>
- Bowen, N. L. (1912). The order of crystallization in igneous rocks. *The Journal of Geology*, 20(5), 457–468. <https://doi.org/10.1086/621991>
- Boyet, M. (2005). ¹⁴²Nd evidence for early (>4.53 Ga) global differentiation of the silicate earth. *Science*, 309(5734), 576–581. <https://doi.org/10.1126/science.1113634>
- Caro, G., Bourdon, B., Wood, B. J., & Corgne, A. (2005). Trace-element fractionation in Hadean mantle generated by melt segregation from a magma ocean. *Nature*, 436(7048), 246–249. <https://doi.org/10.1038/nature03827>
- Corgne, A., Liebske, C., Wood, B. J., Rubie, D. C., & Frost, D. J. (2005). Silicate perovskite-melt partitioning of trace elements and geochemical signature of a deep perovskitic reservoir. *Geochimica et Cosmochimica Acta*, 69(2), 485–496. <https://doi.org/10.1016/j.gca.2004.06.041>
- Corgne, A., & Wood, B. J. (2004). Trace element partitioning between majoritic garnet and silicate melt at 25 GPa. *Physics of the Earth and Planetary Interiors*, 143–144, 407–419. <https://doi.org/10.1016/j.pepi.2003.08.012>
- Creasy, N., Girard, J., Eckert, J. O., Jr, & Lee, K. K. M. (2020). The role of redox on bridgmanite crystal chemistry and calcium speciation in the lower mantle. *Journal of Geophysical Research: Solid Earth*, 125(10), 418. <https://doi.org/10.1029/2020JB020783>
- Dziewonski, A. M., Lekic, V., & Romanowicz, B. A. (2010). Mantle anchor structure: An argument for bottom up tectonics. *Earth and Planetary Science Letters*, 299(1–2), 69–79. <https://doi.org/10.1016/j.epsl.2010.08.013>
- Elkins-Tanton, L. T. (2012). Magma oceans in the inner solar system. *Annual Review of Earth and Planetary Sciences*, 40(1), 113–139. <https://doi.org/10.1146/annurev-earth-042711-105503>
- Fiquet, G., Auzende, A. L., Siebert, J., Corgne, A., Bureau, H., Ozawa, H., & Garbarino, G. (2010). Melting of peridotite to 140 gigapascals. *Science*, 329(5998), 1516–1518. <https://doi.org/10.1126/science.1192448>
- Garnero, E. J., & Jeanloz, R. (2000). Fuzzy patches on the Earth's core-mantle boundary? *Geophysical Research Letters*, 27(17), 2777–2780. <https://doi.org/10.1029/2000gl008498>
- Garnero, E. J., & McNamara, A. K. (2008). Structure and dynamics of Earth's lower mantle. *Science*, 320(5876), 626–628. <https://doi.org/10.1126/science.1148028>
- Hirose, K., Shimizu, N., van Westrenen, W., & Fei, Y. W. (2004). Trace element partitioning in Earth's lower mantle and implications for geochemical consequences of partial melting at the core-mantle boundary. *Physics of the Earth and Planetary Interiors*, 146(1–2), 249–260. <https://doi.org/10.1016/j.pepi.2002.11.001>
- Ito, E. (2007). *Theory and practice—Multianvil cells and high-pressure experimental methods treatise on geophysics* (Vol. 2, pp. 197–230). Elsevier. <https://doi.org/10.1016/b978-044452748-6.00036-5>
- Jung, D. Y., & Schmidt, M. W. (2011). Solid solution behavior of CaSiO₃ and MgSiO₃ perovskites. *Physics and Chemistry of Minerals*, 38(4), 311–319. <https://doi.org/10.1007/s00269-010-0405-0>
- Kato, T., Ringwood, A. E., & Irifune, T. (1988a). Constraints on element partition coefficients between MgSiO₃ perovskite and liquid determined by direct measurements. *Earth and Planetary Science Letters*, 90(1), 65–68. [https://doi.org/10.1016/0012-821X\(88\)90111-2](https://doi.org/10.1016/0012-821X(88)90111-2)
- Kato, T., Ringwood, A. E., & Irifune, T. (1988b). Experimental determination of element partitioning between silicate perovskites, garnets and liquids: Constraints on early differentiation of the mantle. *Earth and Planetary Science Letters*, 89(1), 123–145. [https://doi.org/10.1016/0012-821X\(88\)90038-6](https://doi.org/10.1016/0012-821X(88)90038-6)
- Kogiso, T., Hirose, K., & Takahashi, E. (1998). Melting experiments on homogeneous mixtures of peridotite and basalt: Application to the genesis of ocean island basalts. *Earth and Planetary Science Letters*, 162(1–4), 45–61. [https://doi.org/10.1016/s0012-821x\(98\)00156-3](https://doi.org/10.1016/s0012-821x(98)00156-3)
- Kuwahara, H., Nomura, R., Nakada, R., & Irifune, T. (2018). Simultaneous determination of melting phase relations of mantle peridotite and mid-ocean ridge basalt at the uppermost lower mantle conditions. *Physics of the Earth and Planetary Interiors*, 284, 36–50. <https://doi.org/10.1016/j.pepi.2018.08.012>
- Labrosse, S., Hernlund, J. W., & Coltice, N. (2007). A crystallizing dense magma ocean at the base of the Earth's mantle. *Nature*, 450(7171), 866–869. <https://doi.org/10.1038/nature06355>
- Liebske, C., Corgne, A., Frost, D. J., Rubie, D. C., & Wood, B. J. (2005). Compositional effects on element partitioning between Mg-silicate perovskite and silicate melts. *Contributions to Mineralogy and Petrology*, 149(1), 113–128. <https://doi.org/10.1007/s00410-004-0641-8>
- Liebske, C., & Frost, D. J. (2012). Melting phase relations in the MgO-MgSiO₃ system between 16 and 26 GPa implications for melting in Earth's deep interior. *Earth and Planetary Science Letters*, 345–348(C), 159–170. <https://doi.org/10.1016/j.epsl.2012.06.038>
- Mukhopadhyay, S. (2012). Early differentiation and volatile accretion recorded in deep-mantle neon and xenon. *Nature*, 486(7401), 101–104. <https://doi.org/10.1038/nature11141>
- Mundl, A., Touboul, M., Jackson, M. G., Day, J. M. D., Kurz, M. D., Lekic, V., et al. (2017). Tungsten-182 heterogeneity in modern ocean island basalts. *Science*, 356(6333), 66–69. <https://doi.org/10.1126/science.aal4179>
- Murthy, V. R. (1991). Early differentiation of the earth and the problem of mantle siderophile elements: A new approach. *Science*, 253(5017), 303–306. <https://doi.org/10.1126/science.253.5017.303>
- Nakajima, M., & Stevenson, D. J. (2015). Melting and mixing states of the Earth's mantle after the moon-forming impact. *Earth and Planetary Science Letters*, 427(C), 286–295. <https://doi.org/10.1016/j.epsl.2015.06.023>
- Nomura, R., Zhou, Y., & Irifune, T. (2017). Melting phase relations in the MgSiO₃-CaSiO₃ system at 24 GPa. *Progress in Earth and Planetary Sciences*, 4(1), 1–11. <https://doi.org/10.1186/s40645-017-0149-2>
- Ohtani, E., Nagata, Y., Suzuki, A., & Kato, T. (1995). Melting relations of peridotite and the density crossover in planetary mantles. *Chemical Geology*, 120(3–4), 207–221. [https://doi.org/10.1016/0009-2541\(94\)00139-y](https://doi.org/10.1016/0009-2541(94)00139-y)
- Piet, H., Badro, J., & Gillet, P. (2017). Geochemical constraints on the size of the moon-forming giant impact. *Geophysical Research Letters*, 44(23), 11770–11777. <https://doi.org/10.1002/2017GL075225>
- Piet, H., Badro, J., Nabeil, F., Dennenwaldt, T., Shim, S.-H., Cantoni, M., et al. (2016). Spin and valence dependence of iron partitioning in Earth's deep mantle. *Proceedings of the National Academy of Sciences of the United States of America*, 113(40), 11127–11130. <https://doi.org/10.1073/pnas.1605290113>
- Rizo, H., Boyet, M., Blichert-Toft, J., O'Neil, J., Rosing, M. T., & Paquette, J.-L. (2012). The elusive Hadean enriched reservoir revealed by ¹⁴²Nd deficits in Isua Archean rocks. *Nature*, 491(7422), 96–100. <https://doi.org/10.1038/nature11565>

- Rizo, H., Boyet, M., Blichert-Toft, J., & Rosing, M. (2011). Combined Nd and Hf isotope evidence for deep-seated source of Isua lavas. *Earth and Planetary Science Letters*, *312*(3–4), 267–279. <https://doi.org/10.1016/j.epsl.2011.10.014>
- Solomatov, V. (2015). *9.04 magma oceans and primordial mantle differentiation treatise on geophysics* (Vol. 9, pp. 81–104). Elsevier. <https://doi.org/10.1016/b978-0-444-53802-4.00155-x>
- Solomatov, V. S., & Stevenson, D. J. (1993). Nonfractional crystallization of a terrestrial magma ocean. *Journal of Geophysical Research*, *98*(E3), 5391–5406. <https://doi.org/10.1029/92je02579>
- Sossi, P. A., Burnham, A. D., Badro, J., Lanzirrotti, A., Newville, M., & O'Neill, H. S. C. (2020). Redox state of Earth's magma ocean and its Venus-like early atmosphere. *Science Advances*, *6*(48), eabd1387. <https://doi.org/10.1126/sciadv.abd1387>
- Thorne, M. S., & Garnero, E. J. (2004). Inferences on ultralow-velocity zone structure from a global analysis of SPdKS waves. *Journal of Geophysical Research*, *109*(B8), B08301. <https://doi.org/10.1029/2004JB003010>
- Torsvik, T. H., Burke, K., Steinberger, B., Webb, S. J., & Ashwal, L. D. (2010). Diamonds sampled by plumes from the core-mantle boundary. *Nature*, *466*(7304), 352–355. <https://doi.org/10.1038/nature09216>
- Touboul, M., Puchtel, I. S., & Walker, R. J. (2012). ¹⁸²W evidence for long-term preservation of early mantle differentiation products. *Science*, *335*(6072), 1065–1069. <https://doi.org/10.1126/science.1216351>
- Vitos, L., Magyari-Köpe, B., Ahuja, R., Kollár, J., Grimvall, G., & Johansson, B. (2006). Phase transformations between garnet and perovskite phases in the Earth's mantle: A theoretical study. *Physics of the Earth and Planetary Interiors*, *156*(1–2), 108–116. <https://doi.org/10.1016/j.pepi.2006.02.004>
- Walter, M. J., & Trønnes, R. G. (2004). Early earth differentiation. *Earth and Planetary Science Letters*, *225*(3–4), 253–269. <https://doi.org/10.1016/j.epsl.2004.07.008>
- Walter, M. J., Trønnes, R. G., Armstrong, L. S., Lord, O. T., Caldwell, W. A., & Clark, S. M. (2006). Subsolidus phase relations and perovskite compressibility in the system MgO-AlO_{1.5}-SiO₂ with implications for Earth's lower mantle. *Earth and Planetary Science Letters*, *248*(1–2), 77–89. <https://doi.org/10.1016/j.epsl.2006.05.017>

References From the Supporting Information

- Akahama, Y., & Kawamura, H. (2010). Pressure calibration of diamond anvil Raman gauge to 410 GPa. *Journal of Physics: Conference Series*, *215*, 012195. <https://doi.org/10.1088/1742-6596/215/1/012195>
- Andraut, D., Petitgirard, S., Lo Nigro, G., Devidal, J. L., Veronesi, G., Garbarino, G., & Mezouar, M. (2012). Solid-liquid iron partitioning in Earth's deep mantle. *Nature*, *487*(7407), 354–357. <https://doi.org/10.1038/nature11294>
- Nomura, R., Ozawa, H., Tateno, S., Hirose, K., Hernlund, J., Muto, S., et al. (2011). Spin crossover and iron-rich silicate melt in the Earth's deep mantle. *Nature*, *473*(7346), 199–202. <https://doi.org/10.1038/nature09940>
- Pradhan, G. K., Fiquet, G., Siebert, J., Auzende, A. L., Morard, G., Antonangeli, D., & Garbarino, G. (2015). Melting of MORB at core-mantle boundary. *Earth and Planetary Science Letters*, *431*, 247–255. <https://doi.org/10.1016/j.epsl.2015.09.034>